BNL-108452-2015-JA

Enhanced Electrocatalytic Activity and Stability of Pd_3V/C Nanoparticles by a Trace Amount of Pt Decoration for the Oxygen Reduction Reaction

Sufen Liu,[a] Lili Han,[b,c] Jing Zhu,[a] Weiping Xiao,[a] Jie Wang,[a] Hongfang Liu,[a] Huolin Xin,[b,c] and Deli Wang*[a]

[a] Key Laboratory for Large-Format Battery Materials and System, Ministry of Education, School of Chemistry and Chemical Engineering, Huazhong University of Science&Technology, Wuhan, 430074, P.R. China. E-mail: wangdl81125@hust.edu.cn.

[b] Center for Functional Nanomaterials, Brookhaven National Laboratory, Upton, NY 11973, USA

[c] Department of Materials Science and Engineering, Stony Brook University, Stony Brook, NY, 11794, USA

Carbon supported Pd_3V bimetallic alloy nanoparticles (Pd_3V/C) have been successfully synthesized via a simple impregnation-reduction method, followed by high temperature treatment under H_2 atmosphere. Electrochemical test reveals that the half-wave potential of Pd_3V/C-500 shifts positively of 40 mV compared with Pd/C. However, the catalytic activity of Pd_3V/C-500 suffers from a serious degradation after 1 K cycles. By a spontaneous displacement reaction or co-reduction method, a trace amount of Pt has been decorated on the surface or inside of Pd_3V/C nanoparticles. The catalytic activity and stability of Pd_3V@Pt/C and Pt-Pd_3V/C catalysts for the oxygen reduction reaction (ORR) enhance significantly, which is comparable to commercial Pt/C. In addition, the Pt mass activity of Pd_3V@Pt/C and Pt-Pd_3V/C improve by factors of 10.9 and 6.5 at 0.80 V relative to Pt/C. Moreover, Pt-decorated Pd_3V/C nanoparticles show almost no obvious morphology change after durability test, because of the Pt-rich shell plays an important role in preventing degradation.

1 Introduction

Proton-Exchange Membrane Fuel Cells (PEMFCs) have long been recognized as one of promising alternative power sources for mobile and transportation application because of their high energy efficiency and environment friendly merits[1-6]. However, one of the obstacles for widespread application of PEMFCs is the sluggish cathodic reaction[7-9]. Pt is commonly used as electrocatalytic material in both anode and cathode electrode. While the high cost and scarcity of Pt hinder its scale production[10, 11]. Furthermore, Pt endures a high overpotential in the ORR and is susceptible to be poisoned when meeting the reactive intermediates (CO, HCHO, etc)[12-14]. Therefore, it is necessary to explore non-Pt-based catalysts so as to ameliorate these disadvantages. Recently, Pd and Pd-based materials have attracted much attention since Pd possesses similar properties to Pt, while the cost of Pd is much lower and reservation is more abundant than that of Pt[15]. However, the catalytic activity and stability of Pd-based materials need to be further improved.

A considerable effort has been made to improve the kinetic activity of the ORR on Pd catalysts. From a theoretical perspective, the down shift of the Pd weighted d-band center weakens the adsorption energy of oxygen to Pd[16]. Actually, a number of researches have shown that the activity of ORR on Pd alloyed with some 3*d*-transition metals (e.g. Cr, Fe, Co, Ni, Cu, et al.) is much higher than on pure Pd and is comparable to that on Pt[17-21]. For examples, Pd_3Co/C exhibited the best electrocatalytic activity for ORR among the Pd-Co system[22, 23]. Adzic group reported that the ORR activity of Pd-Fe alloy electrocatalyst surpassed Pt/C[24]. Recently, Pd-Co-Au and Pd-Co-Mo catalysts have been investigated and exhibited slightly higher catalytic activity than the commercial

Pt catalyst for ORR in PEMFC[17, 25]. By incorporating a second metal in Pd lattice, there are two ways to influence the catalytic activity of Pd for ORR: hindering palladium oxide formation and stabilizing Pd naonparticles[26]. Above studies indicate that Pd-based catalysts would enhance the commercial viability of the fuel cell technology. Vanadium (V) as a 3*d*-transition metal could provide similar enhancement effect for Pd like other transition metals. However, the related studies on Pd-V based catalysts are rare[27, 28], probably because of the relative negative standard electrode potential of V^{2+}/V (-1.175 vs. SHE), making it difficult to be reduced to form alloy.

Herein, we report a simple impregnation reduction method for synthesizing Pd_3V alloy nanoparticles supported on Vulcan XC-72 carbon material. The synthetic strategy includes two crucial steps, the reduction stage and post-treatment process. The Pd_3V/C alloy nanoparticles were first obtained by reducing the precursors under flowing H_2 in tube furnace at 300 ^oC. The sample was then heat-treated under H_2 atmosphere at 500 ^oC and 700 ^oC, respectively. Electrochemical test indicates Pd_3V/C-500 nanoparticles exhibit enhanced electrocatalytic activity for the ORR relative to Pd/C. However, it suffers from a serious degradation after long-term cycling. To enhance the stability of Pd_3V/C-500 catalysts for ORR, a small amount of Pt was decorated on the surface or inside of Pd_3V/C-500 nanoparticles via a spontaneous displacement reaction (denoted as Pd_3V@Pt/C) or co-reduction method (denoted as Pt-Pd_3V/C). As expected, the Pt-decorated Pd_3V/C nanoparticles not only exhibit much more durable and stable activity, but also enhanced catalytic activity for ORR, comparable with Pt/C.

2 Experimental Section

2.1 Synthesis of Pd_3V/C, Pd_3V@Pt and Pt-Pd_3V/C catalysts

Pd_3V/C nanoparticles were synthesized by using a simple impregnation reduction method[29, 30] as illustrated in Fig. S1 (Fig. S1, ESI†). In detail, 3.5 mL of 0.108 M $PdCl_2$ solution and 1.3 mL of 0.1 M VCl_3 solution were added in a 25 mL beaker and ultrasonicated to form a homogeneous solution. 153.6 mg of Vulcan XC-72 carbon support were then dispersed in the solution. By interchanging magnetic stirring at 60 ^oC with ultrasonic blending, a smooth thick slurry was formed. After dried at 60 ^oC in vacuum oven for 10 h, the resulting precursor was grounded in an agate mortar, heated in a tube furnace at 300 ^oC under flowing H_2 (30 mL min^{-1}) for 2 h and then cooled to room temperature in N_2 (100 mL min^{-1}) atmosphere for use. The material obtained at 300 ^oC is denoted as Pd_3V/C-300. To increase the alloying degree of Pd_3V/C-300 nanoparticles, a post heat treatment was performed at 500 ^oC and 700 ^oC, which is denoted as Pd_3V/C-500 and Pd_3V/C-700, respectively.

Pd_3V@Pt/C nanoparticles were obtained via a spontaneous displacement reaction. In detail, 50 mg of as-prepared Pd_3V/C-500 sample was dispersed in a certain amount of K_2PtCl_4 solution by controlling the Pt to Pd nominal atomic ratio 1:30. After ultrasonic blending, the suspension was heated at 60^oC under magnetic stirring for 2 h. Then, it was centrifuged with ultra-pure water and dried in a vacuum oven for 10 h.

Pt-Pd_3V/C catalyst was synthesized by using a co-reduction method. In detail, 0.88 mL of 0.108 M $PdCl_2$ solution, 0.33 mL of 0.1 M VCl_3 solution and a certain amount of K_2PtCl_4 solution (the nominal atomic ratio of Pt to Pd is 1:30) were added to a beaker. 37.8 mg of Vulcan XC-72 carbon support were dispersed in the blended solution. The other processes were similar to Pd_3V/C as mentioned above. Finally, the powder was reduced at 300 ^oC under flowing H_2 for 2 h and annealed at 500 ^oC for 10 h.

As a comparison, Pd/C catalyst with Pd weight percentage of 20 % was synthesized via the same procedure at 150 °C for 2 h flowing H_2.

2.2 Material Characterization

XRD patterns of the as-prepared catalysts were obtained on an X'Pert PRO diffractometer using a Cu Kα radiation source. The diffraction patterns were collected from 15° to 85° at a scanning rate of 4 °/min. TEM measurements were performed on a Tecnai G320TEM operated at 300 kV.

2.3 Electrochemical Measurements

Electrochemical measurements were conducted in 0.1 M $HClO_4$ solution at room temperature (298K) on an electrochemical workstation (CHI760Instruments) with a rotating disk electrode system (Pine Research Instrumentation, USA). At first, 5 mg of the as-prepared sample was dispersed in 1 mL 0.1 % Nafion solution (diluted with isopropyl alcohol) and was sonicated until it formed homogeneous ink. 7.8 μL of the solution was dropped uniformly onto a glassy carbon electrode (diameter of 5 mm). After solvent evaporation, a thin layer of catalyst remained on the surface of electrode to serve as working electrode. A Pt wire served as counter electrode and reversible hydrogen electrode (RHE) in the same electrolyte was used as reference electrode. All of the electrodes were pre-treated by cycling prior to electrochemical test to remove surface contamination and all potentials are referred to RHE. Cyclic voltammograms (CV) and CO-stripping voltammetry were measured in N_2-saturated 0.1 M $HClO_4$ solution. ORR was conducted in O_2-saturated 0.1 M $HClO_4$ solution at a scan rate of 5 mV s^{-1} and rotation rate of 1600 rpm.

3 Results and Discussion

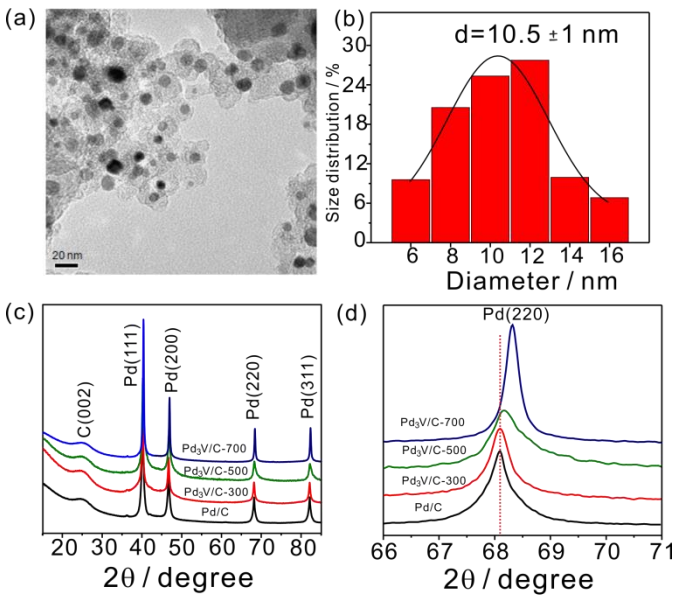

Fig. 1 (a) TEM image of Pd_3V/C-500. (b) Particle size distribution of Pd_3V/C-500. (c) XRD patterns of Pd/C and Pd_3V/C series catalysts. (d) Expanded Pd (220) diffraction peaks.

Fig. 1a shows a typical TEM image of Pd_3V/C-500 catalyst. It can be seen that the particles

exhibit a uniform spherical-like morphology and well dispersed on the surface of carbon support. Fig. 1b presents the histogram of particle size distribution of Pd_3V/C-500 nanoparticles. A narrow size distribution between 6 and 16 nm and the average particle size value of 10.5 nm was displayed by examination of more than 300 particles in an arbitrarily chosen area of TEM images.

Table 1 the results of XRD and electrochemical analysis

Sample	Crystallite size (nm)	Lattice parameter(nm)	Strain(%)	$E_{1/2}$(V)	Massactivity (mA μg_{Pd}^{-1})
Pd/C	15.0	0.3891	----	0.765	0.2567
Pd_3V/C-300	12.5	0.3888	0.08	0.761	0.2221
Pd_3V/C-500	12.8	0.3885	0.15	0.805	1.5143
Pd_3V/C-700	21.2	0.3871	0.51	0.781	0.4183

The XRD patterns of Pd/C and Pd_3V/C alloys after different high-temperature pretreatment are shown in Fig. 1c. The XRD data were analyzed using JADE6.0 software after subtracting background and stripping the Kα2 pattern. The broad peak at around 25° is attributed to the carbon support. The other diffraction peaks located at 40.08°, 46.64°, 68.12° and 82.09°, are correspond to the (111), (200), (220) and (311) planes of Pd with face centered cubic (fcc) phase. The peaks positions of Pd_3V/C-500 and Pd_3V/C-700 shift to higher angle and the peaks become sharper compared to Pd/C and Pd_3V/C-300, which can be clearly seen in the expanded (220) diffraction peaks displayed in Fig. 1d. The shift of peaks position indicates the alloy formation between Pd and V and the smaller atomic radius V incorporated into Pd fcc structure, resulting in a contracted Pd lattice. Due to most of V alloyed with Pd, the amount of V or VO_x is too small to be detected from XRD. The narrower of diffraction peaks indicates the larger particle size with increasing the temperature. The crystallite size and lattice parameter were calculated based on the diffraction peak (220) position by using Debye−Scherrerequation[31]. As shown in Table 1, the domain size of Pd_3V/C-500 is about 12.8 nm, which is closed to the average particle size obtained from the TEM measurement. Pd_3V/C-700 showed a considerable lattice contraction with the value of 0.51 %, while the particle size increased apparently, resulting from sintering after higher temperature treatment.

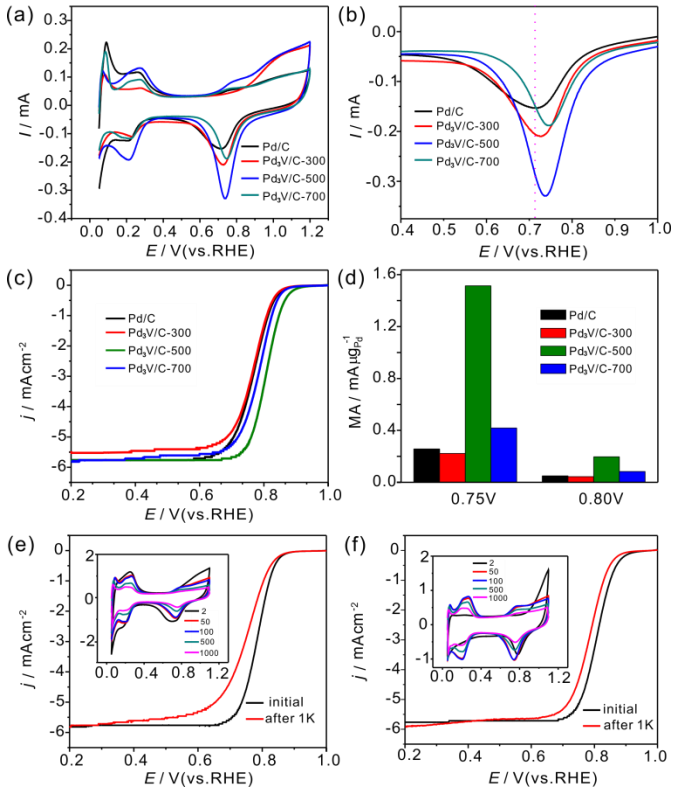

Fig. 2 (a) CVs of Pd/C and Pd_3V/C series catalysts in N_2- saturated 0.1 M $HClO_4$ solution at a scan rate of 50 mV s^{-1}. (b) Enlarged region of Pd oxides reduction peaks. (c) ORR polarization curves comparison of different catalysts in O_2-saturated 0.1 M $HClO_4$ solution at a scan rate of 5 mV s^{-1} and rotation rate of 1600 rpm. (d) Mass activity comparison at 0.75 V and 0.80 V. The ORR polarization curves on Pd/C. (e) and Pd_3V/C-500 (f) before and after 1 K cycles. The insets show the CV curves changing during cycling.

The CVs of different catalysts were performed in N_2-saturated 0.1 M $HClO_4$ solution at room temperature. All of the electrocatalysts were first pretreated by CV potential cycling between 0.05 to 1.2 V for 50 cycles at a scan rate of 50 mV s^{-1} to remove contaminants from the sample surface. Fig. 2a compared the CVs of Pd/C and Pd-V/C series catalysts. It can be seen that the onset potential of surface oxides formation and the reduction of surface oxides changes with various temperature. The enlarged region of Pd oxides reduction peaks in Fig. 2b clearly show that peaks potential on Pd-V/C series catalyst positively shift compared with Pd/C and the shifts change with temperature. It is reported that the peak potential for oxides reduction reflects the binding strength of oxygen on metal surface[23]. The more positive peak potential indicates the weaker oxygen adsorption strength. The ORR polarization curves on different electrodes are shown in Fig. 2c. The half-wave potential of Pd_3V/C-500 shows a 40 mV positive shift compared to Pd/C, indicating the faster ORR kinetic on Pd_3V/C-500 catalysts. The enhanced electrocatalytic activity is attributed to the bi-functional effect and the electronic interaction between Pd and V in the alloy[32, 33]. The unsatisfactory catalytic activity of Pd_3V/C-300 and Pd_3V/C-700 is probably due to lower degree of alloy or larger particle size, which is consistent with the result of XRD shown in Table 1. More importantly, the Pd mass activity of Pd_3V/C-500 is almost 6 times and 4 times with respect to Pd/C at 0.75 V and 0.80 V as shown in Fig. 2d. Above analysis indicated that Pd_3V/C-500 provides the highest electrocatalytic

activity for the ORR among Pd/C and Pd-V/C catalysts.

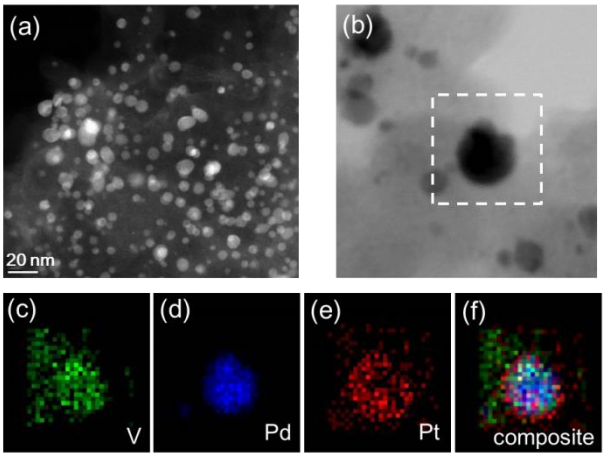

Fig. 3 (a) Overview DF-STEM image of Pd_3V@Pt/C nanoparticles before durability test. (b) BF-STEM image of one Pd_3V@Pt/C nanoparticle that was spectroscopically imaged. EELS elemental mapping of V (c), Pd (d), Pt (e) and the composite of V, Pd and Pt (f).

The durability of Pd/C and Pd_3V/C-500 were evaluated by applying potential cycling between 0.05 V and 1.10 V at a scan rate of 50 mV s^{-1} for 1 K cycles in 0.1 M $HClO_4$ solution. Fig. 2e and f show the ORR polarization curves on Pd/C and Pd_3V/C-500 before and after 1 K cycles. The insets compare the CV curves change during cycling. The significant oxidation current above 1.1 V in CV curve of Pd_3V/C-500 in the second circle is attributed to the oxidation of V. The inhibited hydrogen desorption in the hydrogen region probably caused by the incorporated V. For Pd/C, the half-wave potential is about 36 mV shift to lower potential, while only 22 mV potential shift on Pd_3V/C-500 catalyst after 1 K cycles, indicating the more durable on Pd_3V/C-500 for ORR. Although Pd_3V/C-500 catalyst exhibits enhanced electrocatalytic activity and stability for ORR relative to Pd/C, it need to be further improved for practical application.

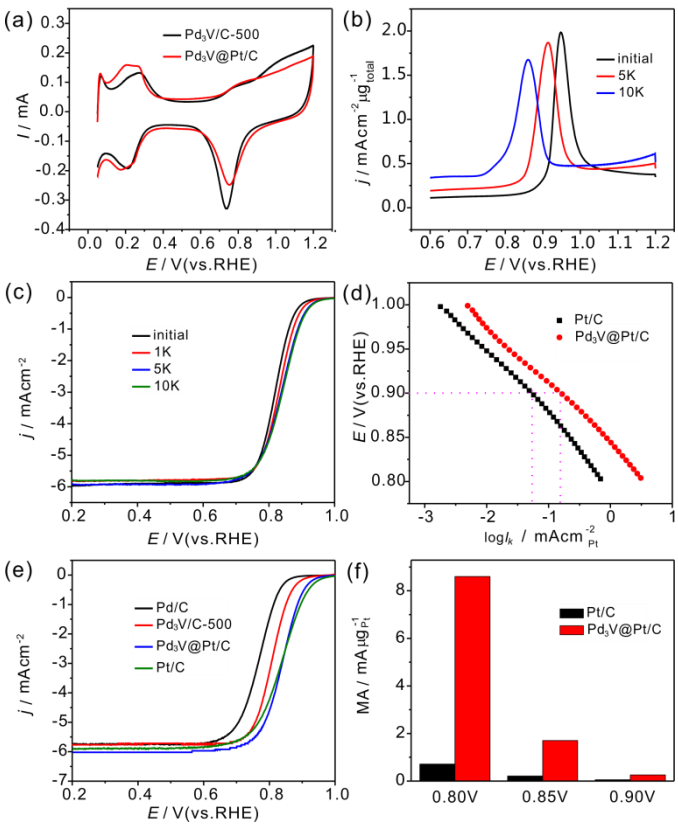

Fig. 4 (a) CVs of Pd_3V/C-500 and Pd_3V@Pt/C. (b) CO stripping voltammetry of Pd_3V@Pt/C at a scan rate of 50 mV s^{-1}. (c) ORR polarization curves on Pd_3V@Pt/C after different potential cycles. (d) Specific activity comparison of Pd_3V@Pt/C and Pt/C. (e) Comparison of ORR polarization curves on different catalysts. (f) Mass activity comparison of Pd_3V@Pt/C and Pt/C at 0.80 V, 0.85 V and 0.90 V.

It is reported that a monolayer Pt decorated on the surface of Pd-based materials enhance the activity and stability for ORR[34-37]. Traditional strategy for Pt monolayer decoration is Cu underpotential deposition (UPD)[38, 39]. In this study, two strategies were used to decorate a small amount of Pt on the surface or inside of Pd_3V/C-500 nanoparticles. The content of Pt in both catalysts is very little (Table S1 and Fig. S4, ESI†). One is spontaneous displacement reaction, the other is co-reduction method. Fig. 3a shows overview STEM image of Pd_3V@Pt/C nanoparticles. It can be seen that most of the particles dispersed well on the surface of carbon support. The atomic-scale chemical mapping (Fig. 3c, d, e, and f) of one Pd_3V@Pt/C nanoparticle (Fig. 3b) clearly show Pt-rich shell. The CVs of Pd_3V/C-500 nanoparticles with and without Pt decoration through spontaneous displacement reaction are shown in Fig. 4a. It can be seen that the onset and peak potential of surface oxide reduction positively shift, indicating the weakening of oxygen adsorption after Pt decoration on the surface of Pd_3V/C-500 nanoparticles. To further study the surface structure of Pd_3V@Pt/C nanoparticles, CO stripping voltammetry was performed as shown in Fig. 4b. The onset potentials for CO oxidation shift negatively with cycling and the peak potential of CO is 0.86 V after 10 K cycles, which is comparable to that of pure Pt, suggesting that the surface is more Pt-rich with cycling.

The stability of Pd_3V@Pt/C nanoparticles was evaluated by potential cycling between 0.05 V and 1.1 V for 10 K cycles in N_2-saturated 0.1 M $HClO_4$ solution with a scan rate of 50 mV s^{-1} and

the corresponding ORR polarization curves were recorded. Fig. 4c shows the ORR polarization curves on Pd_3V@Pt/C nanoparticles after different cycles. The half-wave potential shifts positively about 11 mV after 1 K cycles, further shifts about 19 mV after 5 K cycles relative to initial value and stabilized at 0.84 V. The positively shift of half-wave potentials of ORR on Pd_3V@Pt/C nanoparticles probably due to the exposure of more active sites of decorated Pt during cycling. The surface Pt shell stabilized the inside Pd-V nanoparticles as previous literatures[40-42]. In contrast, the half-wave potential of Pt/C suffers a loss of 22 mV after 10 K cycles comparing with its initial value (Fig. S2, ESI†).

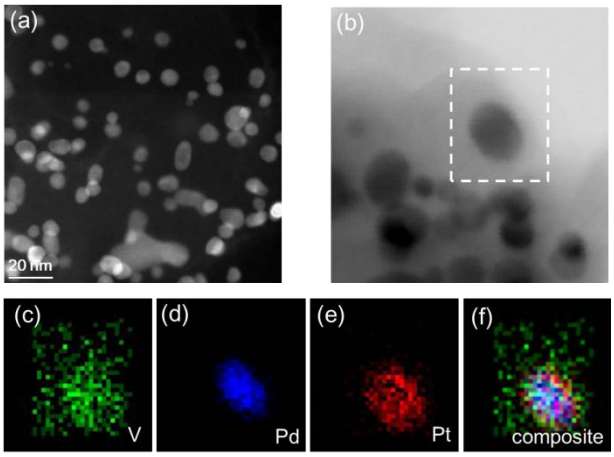

Fig. 5 (a) Overview DF-STEM image of Pd_3V@Pt/C nanoparticles after durability test. (b) BF-STEM image of one Pd_3V@Pt/C nanoparticle that was spectroscopically imaged. EELS elemental mapping of V (c), Pd (d), Pt (e) and the composite of V, Pd and Pt (f).

The specific activity (I_k) comparison of Pd_3V@Pt/C and Pt/C catalysts from 0.8 V to 1.0 V was shown in Fig. 4d, where I_k was normalized to ECSA from the adsorption of CO. The specific activity of Pd_3V@Pt/C was 0.44 mA cm_{Pt}^{-2} at 0.9 V, which is about 1.6 times higher than that on Pt/C. In addition, the comparison of ORR polarization curves of Pd/C, Pd_3V/C-500, Pd_3V@Pt/C and Pt/C in Fig. 4e shows that the half-wave potential of Pd_3V@Pt/C positive shifts more than 30 mV than that on Pd_3V/C-500 and comparable to commercial Pt/C, which could be attributed to more active sites from the Pt shell. To describe the catalytic activity intuitively, kinetic currents were normalized to the amount of Pt to obtain mass activity at 0.80 V, 0.85 V and 0.90 V as shown in Fig. 4f. The mass activity of Pd_3V@Pt/C shows a marked exaltation relative to Pt/C, demonstrating that the nanoparticles could substantially enhance Pt utilization by Pt decoration. In addition, the electron transfer numbers (n) is close to 4 according to the slopes of the Koutecky–Levich plots at 0.775 V, 0.80 V and 0.825 V (Fig. S3, ESI†), indicating almost complete reduction of oxygen to water on the surface of Pd_3V@Pt/C nanoparticles. Moreover, the morphology of Pd_3V@Pt/C catalyst shows no obvious change after potential cycling as shown in Fig. 5a. Pt-rich shell still remained, which plays an important role in providing more active sites and stabilizing the catalytic activity.

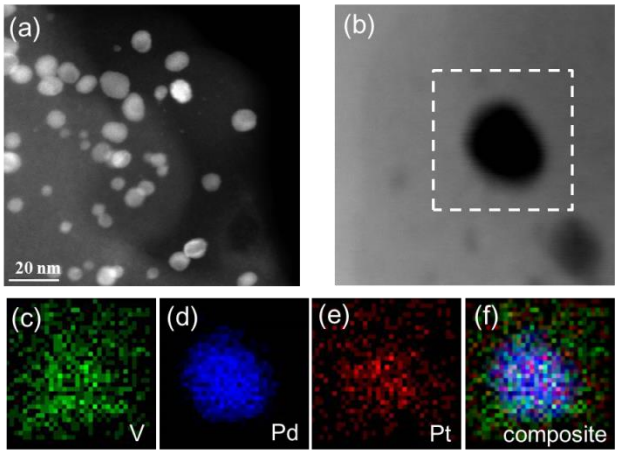

Fig. 6 (a) Overview DF-STEM image of Pt-Pd_3V/C nanoparticles before durability test. (b) BF-STEM image of one Pt-Pd_3V/C nanoparticle that was spectroscopically imaged. EELS elemental mapping of V (c), Pd (d), Pt (e) and the composite of V, Pd and Pt (f).

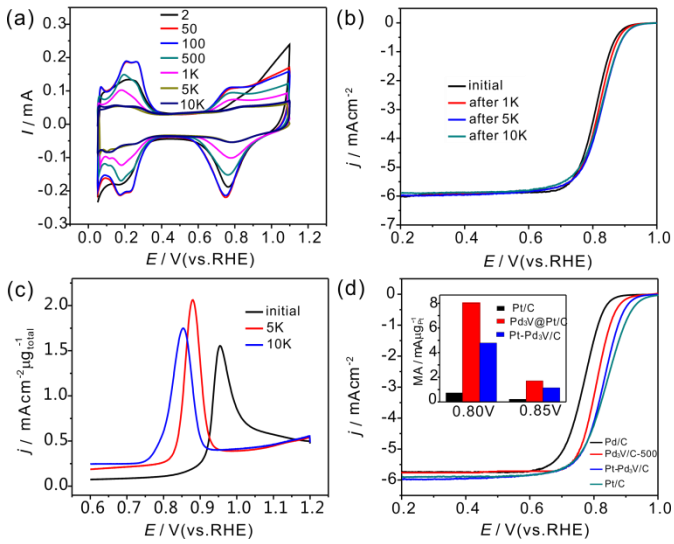

Fig. 7 (a) CV curves of Pt-Pd_3V/C after different cycles. (b) ORR polarization curves on Pt-Pd_3V/C after different cycles. (c) CO stripping voltammetry on Pt-Pd_3V/C at rate of 50 mV s^{-1} after different cycles. (d) The comparison of ORR polarization curves on different electrodes. The inset shows mass activity comparison at 0.8 V and 0.85 V.

On the other hand, Pd_3V/C-500 was decorated by a trace amount of Pt via a co-reduction method to enhance the catalytic activity for ORR. Different from Pd_3V@Pt/C nanoparticles, it can be easily seen that Pt atom evenly distributes in the nanoparticles as shown in Fig. 6. The CVs of Pt-Pd_3V/C nanoparticles after different cycles in N_2-saturated 0.1 M $HClO_4$ solution at a scan rate of 50 mV s^{-1} are displayed in Fig. 7a. The current was first increased due to removing surface contamination and then decreased during 5 K cycles, which is attributed to the dissolution of Pd and V elements during potential cycling. It is noted that the current was stabilized after5 K cycles. The corresponding ORR polarization curves after different cycles are shown in Fig. 7b. It can be seen that the half-wave potentials slightly shifted positive with potential cycling and stabilized after 5 K

cycles, in consistent with CV curves change.

The surface composition after different potential cycling was monitored by CO stripping voltammetry as shown in Fig.7c. It clearly shows that the onset and peak potentials for CO oxidation negative shifted with cycling and was comparable with that of Pt after 10 K, indicating that Pt gradually enriched on the surface of Pt-Pd_3V/C nanoparticles and stabilizing the catalytic activity. Fig. 7d shows the ORR polarization curves comparison on Pd/C, Pd_3V/C-500, Pt-Pd_3V/C and Pt/C. It can be clearly seen that the half-wave potential of Pt-Pd_3V/C catalyst is significant positive shift compared with Pd/C and Pd_3V/C-500, although it is slightly negative than on Pt/C. The Pt mass activity of Pt-Pd_3V/C is about 6.5 and 5.3 times higher than that of Pt/C at 0.80 V and 0.85 V as shown in the inset of Fig. 7d. In order to investigate the origin of the improved durability, the morphology of Pt-Pd_3V/C catalyst was characterized by STEM after stability test in Fig. 8. A Pt-rich shell is formed on the surface obviously, which plays an important role in preventing the degradation of Pt-Pd_3V/C catalyst. The distribution of Pt from EELS elemental mapping is agreed well with the CV curves changing in Fig. 7a.

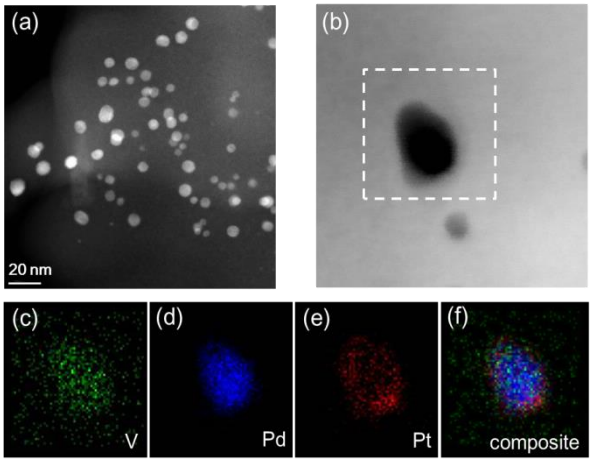

Fig. 8 (a) Overview DF-STEM image of Pt-Pd_3V/C nanoparticles after durability test. (b) BF-STEM image of one Pt-Pd_3V/C nanoparticle that was spectroscopically imaged. EELS elemental mapping of V (c), Pd (d), Pt (e) and the composite of V, Pd and Pt (f).

Above analysis clearly shows that Pd_3V@Pt/C and Pt-Pd_3V/C catalysts both achieve enhanced electrocatalytic activity and stability for ORR compared with Pd_3V/C and Pt/C. When we compare the two decoration methods, Pd_3V@Pt/C catalyst exhibits higher mass activity, which is attributed to the limited utilization of Pt in Pt-Pd_3V/C nanoparticles since a lot of Pt atoms are enfolded in the interior of catalysts and are not completely exposed to the electrolyte as shown in Fig 6c.

Conclusions

In conclusion, we have successfully synthesized Pd_3V/C alloy nanoparticles via an impregnation reduction method. The results show that Pd_3V/C-500 exhibits enhanced ORR electrocatalytic activity and durability than that of Pd/C. The activity of Pd_3V/C-500 nanoparticles is further enhanced by a small amount of Pt via a spontaneous displacement reaction or co-reduction method. Importantly, Pd_3V@Pt/C and Pt-Pd_3V/C catalysts with ultralow amount of Pt provide superior

durability. After potential cycling, the morphology shows almost no obvious change and a Pt-rich shell can be obviously observed, which plays a key role in enhancing the stability of Pd_3V/C nanoparticles. The simple synthetic strategy for catalytic preparation is scalable for mass production and the obtained Pd_3V@Pt/C and Pt-Pd_3V/C electrocatalysts with superior electrochemical performance and excellent stability will possess considerable potential as cathode catalyst in fuel cells application.

Acknowledgements

This work was supported by the National Natural Science Foundation (21306060, 21573083), the Program for New Century Excellent Talents in Universities of China (NCET-13-0237), the Fundamental Research Funds for the Central University (2013TS136 and 2014YQ009). We thank Analytical and Testing Center of Huazhong University of Science & Technology for allowing us to use its facilities. STEM and EELS work was carried out at the Center for Functional Nanomaterials, Brookhaven National Laboratory, which is supported by the U.S. Department of Energy, Office of Basic Energy Sciences, under Contract No.DE-SC0012704.

Notes and references

Electronic Supplementary Information (ESI) available: [details of illustration of the synthesis procedure, electrochemical performance and TGA curve]. See DOI: 10.1039/c000000x/

1. M. M. Liu, R. Z. Zhang and W. Chen, *Chem. Rev.*, 2014, **114**, 5117-5160.
2. S. J. Guo, X. Zhang, W. L. Zhu, K. He, D. Su, A. Mendoza-Garcia, S. F. Ho,G. Lu and S. H. Sun, *J. Am. Chem. Soc.*, 2014, **136**, 15026-15033.
3. A. Sarkar, A. V. Murugan and A. Manthiram, *J. Mater. Chem.*, 2009, **19**, 159-165.
4. J. J. Lv, J. N. Zheng, S. S. Li, L. L. Chen, A. J. Wang and J. J. Feng, *J. Mater. Chem. A*, 2014, **2**, 4384-4390.
5. A. Morozan, B. Jousselme and S. Palacin, *Energy Environ. Sci.*, 2011, **4**, 1238-1254.
6. X. L. Ji, K. T. Lee, R. Holden, L. Zhang, J. J. Zhang, G. A. Botton, M. Couillard and L. F. Nazar, *Nat. Chem.*, 2010, **2**, 286-293.
7. C. X. Xu, Y. Q. Liu, Q. Hao and H. M. Duan, *J. Mater. Chem. A*, 2013, **1**, 13542-13548.
8. M. K. Debe, *Nature*, 2012, **486**, 43-51.
9. H. W. Liang, X. Cao, F. Zhou, C. H. Cui, W. J. Zhang and S. H. Yu, *Adv. Mater.*, 2011, **23**, 1467-1471.
10. E. Antolini, *Energy Environ. Sci.*, 2009, **2**, 915-931.
11. J. N. Zheng, L. L. He, F. Y. Chen, A. J. Wang, M. W. Xue and J. J. Feng, *J. Mater. Chem. A*, 2014, **2**, 12899-12960.
12. G. Hoogers, *Fuel cell technology handbook*, CRC press, 2002.
13. F. Garin, *Catal. Today*, 2004, **89**, 255-268.
14. G. Sievers, S. Mueller, A. Quade, F. Steffen, S. Jakubith, A. Kruth and V. Brueser, *J. Power Sources*, 2014, **268**, 255-260.
15. D. L. Wang, H. L. Xin, Y. C. Yu, H. Wang, E. Rus, D. A. Muller and H. D. Abruna, *J. Am. Chem. Soc.*, 2010, **132**, 17664-17666.

16. J. Greeley and J. K. Nørskov, *Surf. Sci.*, 2005, **592**, 104-111.
17. V. Raghuveer, A. Manthiram and A. J. Bard, *J. Phys. Chem. B*, 2005, **109**, 22909-22912.
18. V. Mazumder, M. Chi, K. L. More and S. Sun, *Angew. Chem. Int. Ed.*, 2010, **49**, 9368-9372.
19. L. Xiong, Y. X. Huang, X. W. Liu, G. P. Sheng, W. W. Li and H. Q. Yu, *Electrochim. Acta*, 2013, **89**, 24-28.
20. T. Cochell, W. Li and A. Manthiram, *J. Phys. Chem. C*, 2013, **117**, 3865-3873.
21. S. Liu, C. Zhang, L. Yuan, J. Bao, W. Tu, M. Han and Z. Dai, *Part. Part. Syst. Char.*, 2013, **30**, 549-556.
22. D. L. Wang, H. L. Xin, R. Hovden, H. S. Wang, Y. C. Yu, D. A. Muller, F. J. DiSalvo and H. D. Abruña, *Nat. Mater.*, 2013, **12**, 81-87.
23. D. L. Wang, H. L. Xin, H. S. Wang, Y. C. Yu, E. Rus, D. A. Muller, F. J. DiSalvo and H. D. Abruña, *Chem. Mater.*, 2012, **24**, 2274-2281.
24. M. H. Shao, K. Sasaki and R. R. Adzic, *J. Am. Chem. Soc.*, 2006, **128**, 3526-3527.
25. J. L. Fernández, V. Raghuveer, A. Manthiram and A. J. Bard, *J. Am. Chem. Soc.*, 2005, **127**, 13100-13101.
26. M. Tarasevich, G. Zhutaeva, V. Bogdanovskaya, M. Radina, M. Ehrenburg and A. Chalykh, *Electrochim. Acta*, 2007, **52**, 5108-5118.
27. S. Y. Ang and D. A. Walsh, *Appl. Catal. B- Environ.*, 2010, **98**, 49-56.
28. D. A. Walsh, J. L. Fernández and A. J. Bard, *J. Electrochem. Soc.*, 2006, **153**, 99-103.
29. D. L. Wang, S. F. Lu and S. P. Jiang, *Electrochim. Acta*, 2010, **55**, 2964-2971.
30. D. L. Wang, L. Zhuang and J. T. Lu, *J. Phys. Chem. C*, 2007, **111**, 16416-16422.
31. S. Y. Shen, T. S. Zhao, J. B. Xu and Y. S. Li, *J. Power Sources*, 2010, **195**, 1001-1006.
32. K. Wang, H. Gasteiger, N. Markovic and P. Ross Jr, *Electrochim. Acta*, 1996, **41**, 2587-2593.
33. P. Christensen, A. Hamnett and G. Troughton, *J. Electroanal. Chem.*, 1993, **362**, 207-218.
34. R. Lin, T. T. Zhao, M. F. Shang, J. Q. Wang, W. C. Tang, V. E. Guterman and J. X. Ma, *J. Power Sources*, 2015, **293**, 274-282.
35. T. Cochell and A. Manthiram, *Langmuir*, 2012, **28**, 1579-1587.
36. R. P. Zhao, Y. Liu, C. Liu, G. G. Xu, Y. Chen, Y. W. Tang and T. H. Lu, *J. Mater. Chem. A*, 2014, **2**, 20855-20860.
37. H. H. Li, S. Y. Ma, Q. Q. Fu, X. J. Liu, L. Wu and S. H. Yu, *J. Am. Chem. Soc.*, 2015,**137**,7863-7868.
38. R. R. Adzic, J. Zhang, K. Sasaki, M. B. Vukmirovic, M. Shao, J. Wang, A. U. Nilekar, M. Mavrikakis, J. Valerio and F. Uribe, *Top. Catal.*, 2007, **46**, 249-262.
39. S. Tominaka, T. Hayashi, Y. Nakamura and T. Osaka, *J. Mater. Chem.*, 2010, **20**, 7175-7182.
40. K. Sasaki, H. Naohara, Y. Choi, Y. Cai, W.-F. Chen, P. Liu and R. R. Adzic, *Nat. Commun.*, 2012, **3**, 1115-1124.
41. G. W. Wang, B. Huang, L. Xiao, Z. D. Ren, H. Chen, D. L. Wang, H. D. Abruña, J. T. Lu and L. Zhuang, *J. Am. Chem. Soc.*, 2014, **136**, 9643-9649.
42. S. Zhang, Y. Z. Hao, D. Su, V. V. Doan-Nguyen, Y. T. Wu, J. Li, S. H. Sun and C. B. Murray, *J. Am. Chem. Soc.*, 2014, **136**, 15921-15924.